

Three-dimensional model of the human platelet integrin $\alpha_{IIb}\beta_3$ based on electron cryomicroscopy and x-ray crystallography

Brian D. Adair* and Mark Yeager**†

*The Scripps Research Institute, Department of Cell Biology, 10550 North Torrey Pines Road, La Jolla, CA 92037; and †Division of Cardiovascular Diseases, Scripps Clinic, 10666 North Torrey Pines Road, La Jolla, CA 92037

Communicated by Donald M. Engelman, Yale University, New Haven, CT, August 19, 2002 (received for review March 7, 2002)

Integrins are a large family of heterodimeric transmembrane signaling proteins that affect diverse biological processes such as development, angiogenesis, wound healing, neoplastic transformation, and thrombosis. We report here the three-dimensional structure at 20-Å resolution of the unliganded, low-affinity state of the human platelet integrin $\alpha_{IIb}\beta_3$ derived by electron cryomicroscopy and single particle image reconstruction. The large ectodomain and small cytoplasmic domains are connected by a rod of density that we interpret as two parallel transmembrane α -helices. The docking of the x-ray structure of the $\alpha_V\beta_3$ ectodomain into the electron cryomicroscopy map of $\alpha_{IIb}\beta_3$ requires hinge movements at linker regions between domains in the crystal structure. Comparison of the putative high- and low-affinity conformations reveals dramatic conformational changes associated with integrin activation.

cell adhesion | transmembrane signaling | membrane proteins | platelets

Integrins are a large family of eukaryotic cell-surface receptors that mediate dynamic interactions between cells and extracellular adhesion molecules (1). They are important for the maintenance of tissue integrity and promotion of cellular migration (2) and play important roles in development, angiogenesis, wound healing, neoplastic transformation, and thrombosis (3–5). Integrins are heterodimeric type I membrane proteins composed of α and β subunits (6). Nineteen α and eight β isoforms have so far been identified in mammals (1). Each α binds only a limited subset of β , and each $\alpha\beta$ pair manifests specific ligand-binding properties (7).

$\alpha_{IIb}\beta_3$ (M_r 235) is one of the best characterized integrins, studied not only for its importance in thrombosis but also as a prototypical integrin (8). $\alpha_{IIb}\beta_3$ is by far the most abundant integrin on the platelet surface (40,000–80,000 copies) and is also present in internal pools (9, 10). The α_{IIb} subunit (M_r 130) undergoes post-translational proteolytic cleavage, producing a 105-kDa extracellular fragment and a 23-kDa fragment containing the single transmembrane span and a 26-residue cytoplasmic domain (8). The two chains are linked by a single disulfide bond. In contrast, β_3 consists of a single polypeptide chain (M_r 95), including a single transmembrane span and a 45-residue cytoplasmic domain.

Previous electron microscopic (EM) images of negatively stained or metal-shadowed $\alpha_{IIb}\beta_3$ complexes revealed a globular domain ≈ 100 Å in diameter and two longer extensions of 140–170 Å (11, 12). When detergent was removed, the protein formed rosettes with an outer radius formed by the globular domain. The molecules were joined at the center by the distal ends of the extensions, suggesting that the latter structures were composed of the hydrophobic domains (11, 12). Consistent with this interpretation, a soluble recombinant form of the extracellular polypeptide revealed a globular domain with shorter tails (13). A similar morphology has been seen in negative-staining studies of protein reconstituted into lipid vesicles where individual heterodimers appear as spikes projecting ≈ 200 Å from the vesicle surface (14).

The integrin $\alpha_V\beta_3$ serves as a viral receptor by binding to an ArgGlyAsp (RGD) motif in the penton base of adenovirus. Elec-

tron cryomicroscopy and difference map analysis were used to derive a 3D map of the recombinant extracellular domain of $\alpha_V\beta_3$ bound to adenovirus (15). The five $\alpha_V\beta_3$ ectodomains were closely packed at the penton base, and each was composed of two domains designated as proximal and distal in relation to the RGD-binding motif on the virus.

$\alpha_{IIb}\beta_3$ can adopt either of two states characterized by a low or high affinity for ligands (6, 8, 16). So-called outside-in signaling occurs as a consequence of binding extracellular ligands, and inside-out signaling is mediated by interactions with proteins bound to the cytoplasmic domains (17, 18). Such bidirectional transmembrane signaling is associated with dramatic conformational changes propagated over ≈ 200 Å. Hantgan *et al.* (19) used light scattering, analytical ultracentrifugation, rotary shadowing EM, and model building to examine the conformational changes associated with outside-in signaling. Binding of ligand-mimetic RGD peptides resulted in separation of the head into two domains and aggregation of oligomers via the stalk domains. Insight into the mechanism for inside-out signaling was recently provided by analysis of a soluble chimeric form of the ectodomain of $\alpha_5\beta_1$, in which the cytoplasmic domains were replaced with an artificial clasp (20). Proteolytic release of the clasp resulted in separation of the stalk domains, which was accompanied by an increase in binding affinity to fibrinogen.

Current models based on EM place the majority of the α and β extracellular domains in the globular head region and assign one projection to each of the stalks that connects to the transmembrane domains. A recent high-resolution crystal structure of the extracellular portion of integrin $\alpha_V\beta_3$ (21) revealed an ovoid “head” and two “tails” composed of 12 domains. Notably, the tails were associated as a single stalk, which was severely bent by $\approx 130^\circ$ with respect to the head.

To further explore integrin structure, we report here the 3D map of unliganded (low-affinity state) $\alpha_{IIb}\beta_3$ derived from single particle reconstruction of detergent-solubilized molecules visualized by electron cryomicroscopy. The 20-Å resolution map reveals the shape and spatial relationships between the domains within the 235-kDa $\alpha_{IIb}\beta_3$ complex and provides the first direct evidence, to our knowledge, for α -helical coiled-coil association of the transmembrane domains in the unliganded state. Comparison with the crystal structure of the $\alpha_V\beta_3$ ectodomain suggests large conformational changes associated with integrin activation.

Materials and Methods

Protein Purification. Five units of outdated human platelets (<8 days from the time of phlebotomy) were obtained from the San Diego Blood Bank (San Diego, CA). All buffers contained 20 mM Tris-HCl, pH 7.0, and all steps were performed at room temperature. Centrifugation at $120 \times g$ removed residual red blood cells, and platelets were isolated from the supernatant by centrifugation

Abbreviations: EM, electron microscopy; EGF, epidermal growth factor.

†To whom correspondence should be addressed. E-mail: yeager@scripps.edu.

at $700 \times g$. The platelets were washed once in buffer containing 150 mM NaCl and 5 mM EDTA, followed by two washes in 150 mM NaCl/1.0 mM CaCl_2 /0.5 mM MgCl_2 . The platelets were resuspended in ≈ 50 ml of buffer and disrupted by sonication (Ultrasonic XL sonifier, microtip, full power, 6×10 sec bursts, Heat Systems/Ultrasonics). The suspension was placed on a 40% (wt/wt) sucrose cushion, and platelet membranes were enriched at the interface by ultracentrifugation in a Beckman Instruments (Palo Alto, CA) SW-28 rotor for 3.5 h at $100,000 \times g$. Material at the 0/40% sucrose interface was washed and then extracted overnight by stirring in buffer containing 5% octyl- β -D-glucopyranoside (Calbiochem), 1.0 mM CaCl_2 , 0.5 mM MgCl_2 , and 25 μM leupeptin. Insoluble material was removed by ultracentrifugation in a Beckman Ti55 for 45 min at $55,000 \times g$. The supernatant was subjected to ion-exchange chromatography (1-ml resource-Q column, Pharmacia) in 1% octyl- β -D-glucopyranoside with a linear gradient of 0–0.35 M NaCl. Western immunoblot analysis was used to identify fractions containing $\alpha_{\text{IIb}}\beta_3$, which were concentrated to <1 ml by ultrafiltration (Centricon 100, Amicon) and subjected to gel-filtration chromatography (Pharmacia superpose-12, 30 cm) in the same buffer lacking NaCl. The purified material was stored at 4°C .

Binding of Echistatin. A 100- μM solution of echistatin (94% pure, not purified further; Sigma) was prepared in Tris buffer as above, lacking EDTA, and stored at -20°C . Four microliters of the purified integrin sample at ≈ 1.5 mg/ml mixed with 0.5 μl of a 5% octyl- β -D-glucopyranoside solution, to which 1.5 μl of the echistatin solution was added, giving a final concentration of 1% octyl- β -D-glucopyranoside. During a 30-min incubation at room temperature, a Pharmacia 8–25% polyacrylamide, continuous gradient, Phast-Gel (2% crosslinking) was incubated for 15 min with a solution of 5% octyl- β -D-glucopyranoside in water, after which excess surface liquid was removed. The buffer reservoir contained 0.88 M L-alanine and 0.25 M Tris, pH 8.8. Four microliters of the integrin–echistatin solution and an equivalent amount of echistatin-free integrin were loaded. Gel standards (Pharmacia HMW-native kit) included thyroglobulin (669 kDa), ferritin (440 kDa), catalase (232 kDa), lactate dehydrogenase (140 kDa), and albumin (66 kDa). Electrophoresis was performed at 10 mA for a total of 240 accumulated volt-hours. The gel was fixed with 10% acetic acid and 50% methanol and was then stained with Coomassie brilliant blue.

Electron Cryomicroscopy and Image Analysis. Samples were prepared in the frozen-hydrated state on holey carbon grids (300-mesh Cu grids rendered hydrophilic by glow discharge in amyl amine) by rapid plunging into liquid ethane (22). Electron cryomicroscopy was performed on a Philips CM200 FEG (Philips Electron Optics/FEL, Eindhoven, The Netherlands) equipped with a Gatan 626 cryostage (Gatan, Pleasanton, CA). Images were recorded on Kodak SO163 film at a nominal magnification of 50,000 by using 100-kV electrons. Defocus values were between -2 and -3 μm . Micrographs were digitized on a SCAI scanner (Zeiss) at 8 bits per pixel and 7 μm per pixel, subsequently averaged to 21 μm per pixel, corresponding to 4.2 \AA per pixel at the level of the specimen. The densitometer parameters were adjusted so that the mean pixel optical density for a negative was set to a mean value of ≈ 127 , over a total range of 0–255.

Image processing was performed with the EMAN software suite (23). Thirty-eight micrographs were selected that displayed minimal drift and astigmatism and had a continuous ring of carbon around the hole. About 4,000 particles were manually selected and extracted as 80×80 pixel images. The optical density histograms for the pixels in each image were scaled to the mean and SD for all images. The contrast transfer function (CTF) parameters for each micrograph were determined from the computed Fourier transform of the carbon surrounding the hole of each micrograph, and phase corrections were then applied to each particle image. The corrected particle images were classified by using factor analysis with *k*-means grouping. The *x,y* origin and rotational orientation

(ω) of the ≈ 50 particles in each group were aligned by eight cycles by using a reference-free method. For each cycle, particles that deviated by 0.8σ from the average were rejected. In general, about one-quarter of the particles were rejected. The 80 resulting classes were split into three groups. The common lines approach was then used to determine the Euler angles for each group of class averages, from which three models were obtained. The starting model for reference-based refinement was an average of these three models. Back projections of this averaged model were computed at 12° intervals. The orientation parameters for each original image were assigned to an Euler angle class by crosscorrelation with the 121 back projections of the model. CTF amplitude corrections were applied to the Fourier transform of each image, and transforms were low-pass filtered to 18\AA^{-1} . The *x,y* origin and rotational orientation (ω) of the particles for each particle were aligned by crosscorrelation with the back projections. The aligned transforms were averaged, and those that exceeded 0.8σ from the average were excluded. The average was then used as a new reference for the next cycle of refinement. The images in each of the 121 classes were subjected to eight rounds of refinement, after which a 3D map was generated. Back projections of this model were then computed for the next cycle of refinement. After 23 subsequent cycles of refinement, the process was halted because the Fourier shell correlation with the previous model did not yield any substantial differences within the resolution cutoff. An estimate of the resolution of the final 3D map was computed by separating the classified images into two groups. Two independent reconstructions were computed without CTF amplitude corrections or low-pass filtering so that the maximum resolution of the map could be determined by Fourier shell correlation. The final 3D map was derived from 3,108 images and visualized by using *o* (29) and AVS software (24). A protein partial specific volume of $0.73 \text{ cm}^3/\text{g}$ was used to set the isosurface threshold that corresponded to the molecular volume.

Results and Discussion

Purification and Structure Analysis. Mature glycosylated human $\alpha_{\text{IIb}}\beta_3$ was isolated from outdated human platelets solubilized in 1% octyl- β -D-glucopyranoside. Native gel electrophoresis revealed a single band migrating with an apparent molecular mass of 284 kDa, indicating that the heterodimer was intact and monodisperse (Fig. 1*a*). The ≈ 5 -kDa disintegrin echistatin (25) exhibits tight binding to $\alpha_{\text{IIb}}\beta_3$, which results in a large conformational change and conversion to a high-affinity state (26, 27). In the presence of echistatin, we observed that $\alpha_{\text{IIb}}\beta_3$ migrated at ≈ 390 kDa (Fig. 1*a*), indicating that the complex was converted from the low- to the high-affinity state. These results are consistent with prior data, indicating that $\alpha_{\text{IIb}}\beta_3$ isolated from human platelets is in the low-affinity state (28).

The detergent–protein complexes were imaged in the frozen-hydrated state by low-dose transmission electron cryomicroscopy (22). Under these conditions, the detergent micelles would not have sufficient contrast to be visualized. Almost 4,000 particles were manually selected from 38 micrographs. The initial 3D model was generated from class averages, with ≈ 50 images in each class, by assigning Euler angles θ , φ , and ω through *sinecorr*s (23). For each of the 24 cycles of refinement, the origin and orientation parameters for each 2D image were derived by crosscorrelation with projections of the 3D model. The resolution of the final reconstruction ($\approx 20 \text{\AA}$) was estimated by Fourier shell correlation of two independent reconstructions, each derived from half of the raw images (Fig. 1*b*). The distribution of the refined orientation angles (Fig. 1*c*) showed that the views covered the entire range of Euler angles, and 102 of 121 views had at least 10 images in the final average.

Multidomained Organization of the $\alpha_{\text{IIb}}\beta_3$ Ectodomain. A surface-shaded 3D map, contoured at 100% of the predicted protein mass (Fig. 2), shows that the overall length of the protein is $\approx 180 \text{\AA}$. The general shape of the ectodomain is similar to images of dried specimens (11–15, 19, 20); however, our map derived from images

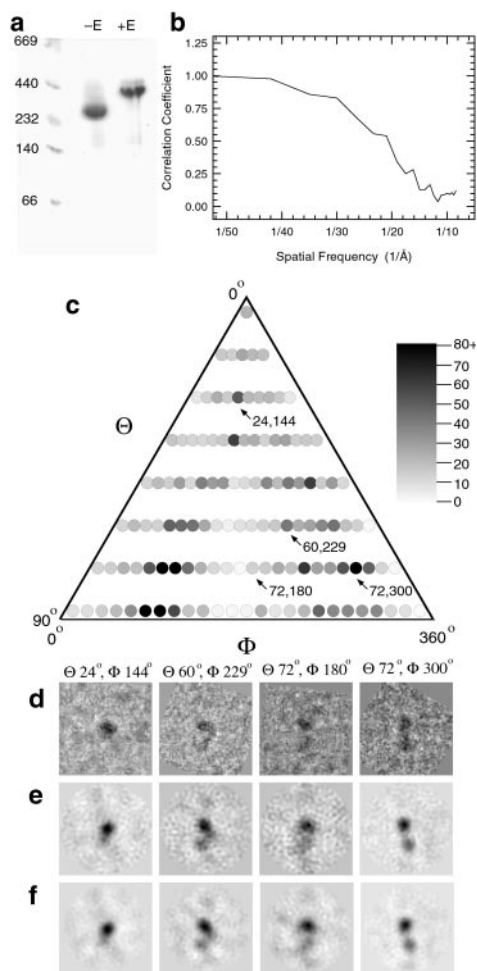


Fig. 1. (a) Native gel electrophoresis of human platelet $\alpha_{IIb}\beta_3$ in the presence of 5% octyl- β -D-glucopyranoside. In the absence of the RGD ligand-mimetic echistatin (-E), the purified complex migrated with an apparent molecular mass of 284 kDa, which shifts to 390 kDa in the presence of echistatin (+E). The locations of molecular mass standards are indicated at the left. (b) Fourier shell correlation to determine map resolution. The total data set was divided into two equal groups. The particles in each data set were independently aligned with projections of the final model, and two independent maps were correlated in Fourier space. The curve crosses the 50% threshold at ≈ 20 -Å resolution. (c) Histogram of the raw images in each view of the final model. Images were aligned translationally (x and y) and rotationally in plane (ω), and each particle was assigned to the group to which it best correlated (23). Each circle represents a projection of the final model for a given θ and ϕ value. The number of particles in each group is represented by a linear gray scale with a value of 1 (black) representing 80 or more in the group and a value of 0 (white), no particles in the group. The distribution of orientations is not random (χ^2 : $P \ll 0.001$), because two clusters separated by $\approx 180^\circ$ are over-represented. (d) Four representative images and their refined θ and ϕ Euler angles. Two of the image averages are from relatively well populated groups representing a top-down view (24, 144°) and a side view (72, 300°). This side view was probably easy to identify visually because of the double density provided by the head and stalk domains. A third image (60, 229°) is intermediate in population, whereas view (72, 180°) is the least well populated for these four particles. In general, the under-represented views corresponded to projections in which both the stalk and head domains presented maximal cross-sectional area (and hence minimal density) and were thus more difficult to recognize visually. (e) Class averages for the particle orientations shown in d. (f) Back-projections of the final 3D reconstruction according to the same Euler angles. There is progressive increase in the clarity of the images from d to f.

of frozen-hydrated molecules reveals several additional features. The large globular head forms an approximate prolate ellipsoid with major and minor axes of ≈ 95 Å and 60–65 Å, respectively. This domain encloses ≈ 160 kDa or two-thirds of the total mass of the

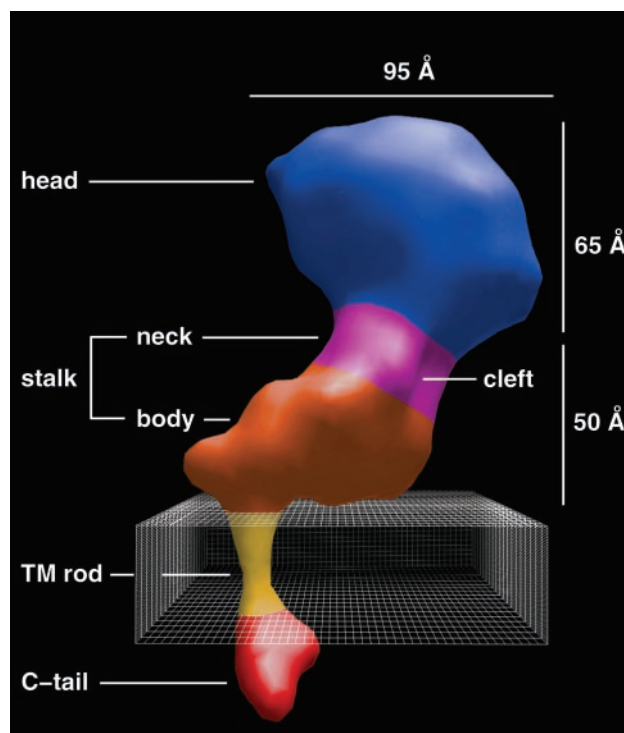


Fig. 2. Surface-shaded 3D density map of the $\alpha_{IIb}\beta_3$ heterodimer at 20-Å resolution. The dimensions and domains are indicated. We presume that the cleft in the neck domain separates the α_{IIb} and β_3 subunits, and the larger lobe of the cytoplasmic domain corresponds to the C tail of the β_3 subunit, which is twice the size of the α_{IIb} C tail. The model has been oriented so that the putative transmembrane rod is roughly perpendicular to the membrane (boxed area, 30 Å thick).

complex and is comparable in shape and size to the ligand-binding portion of the integrin $\alpha_V\beta_3$ ($90 \times 65 \times 80$ Å; ref. 15) and the recent crystal structure of the head domain of $\alpha_V\beta_3$ (19).

The density of the head domain merges with a roughly L-shaped “stalk” domain that accounts for ≈ 80 kDa of protein and is composed of a “neck” and “body” (Fig. 2). The cylindrical neck has a diameter of ≈ 40 Å and a height of ≈ 20 Å. The cleft in the neck may separate the α_{IIb} and β_3 subunits. The body forms an approximately wedge-shaped structure with a length of ≈ 60 Å and a height of ≈ 35 Å. The long axis of the body of $\alpha_{IIb}\beta_3$ is rotated $\approx 60^\circ$ with respect to the long axis of the head.

The body of $\alpha_{IIb}\beta_3$ is angled relative to the transmembrane assembly by $\approx 90^\circ$ (Fig. 2). If the transmembrane rod were oriented perpendicular to the plane of the bilayer, then the bottom surface of the body would form a fairly flat face, roughly parallel to the predicted surface of the membrane. In this orientation, the face could easily interact with lipid headgroups or fully embedded membrane proteins. In addition, the stalk would present a large area for lateral associations with extracellular domains of other membrane proteins.

Implications for Protein–Protein Interactions. The current reconstruction suggests that the extracellular integrin domains may be important for interactions with other proteins. For instance, integrins, including $\alpha_{IIb}\beta_3$, associate with proteins in the transmembrane-4 superfamily (TM4SF or tetraspanins) (30). TM4SF proteins contain two extracellular domains between their eponymous transmembrane domains known as the large and small extracellular loops. The large extracellular loop may extend ≈ 35 Å above the surface of the membrane (31). Crosslinking and mutational evidence suggest direct contact with the large extracellular loop of the tetraspanin CD151 and the α subunit of $\alpha_3\beta_1$ (32), which maps to

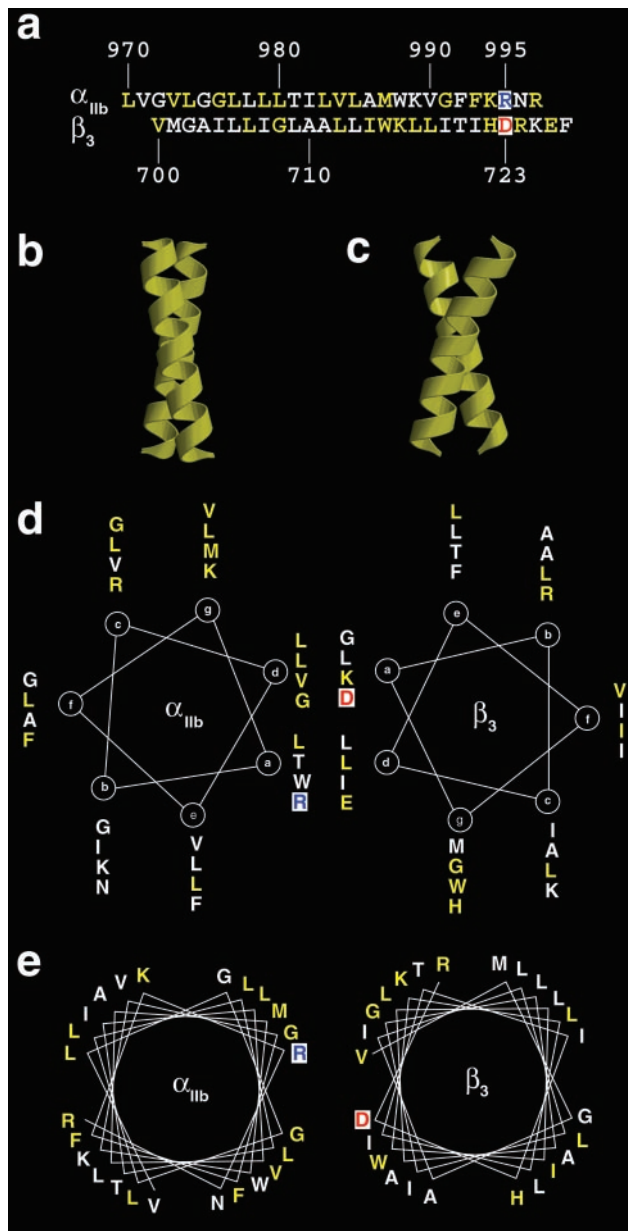


Fig. 3. Models for the packing of integrin transmembrane domains. (a) Predicted transmembrane domains for the human integrin α_{11b} and β_3 subunits based on hydropathy analysis. For the α_{11b} amino acid sequence, the residues colored yellow are identical to residues in the human α_v sequence. For the β_3 sequence, the yellow residues are identical with the human β_1 , β_5 , and β_6 sequences. The residues in the putative ion pair R995 (α_{11b}) and D723 (β_3) are colored blue and red, respectively. Ribbon diagrams for 20-residue α -helices, packing as left- (b) and right-handed (c) coiled-coils. Helical wheel representations (d and e) for the human α_{11b} and β_3 integrin transmembrane sequences. The amino acid positions in the heptad are indicated on the wheel. Absolutely conserved residues are colored yellow. The putative ion pair between R995 (α_{11b}) and D723 (β_3) orients the α -helices with respect to each other. (d) Left-handed coiled-coil (3.5 residues per turn). (e) Right-handed coiled-coil (3.9 residues per turn). The sequence projection is taken from the structure of the transmembrane dimer of glycoporphin A (47). Note that there are substantially more conserved residues at the $\alpha_{11b}\beta_3$ interface when the α -helices are packed in a right-handed fashion.

residues 570–705, some distance in the primary structure from the transmembrane domain at residues 960–985 (33). The tetraspanin CD9 is thought to associate with $\alpha_{11b}\beta_3$ via hydrophobic interactions with the transmembrane domains (34). $\alpha_{11b}\beta_3$ also interacts with the integrin-associated protein (IAP or CD47) that contains five pu-

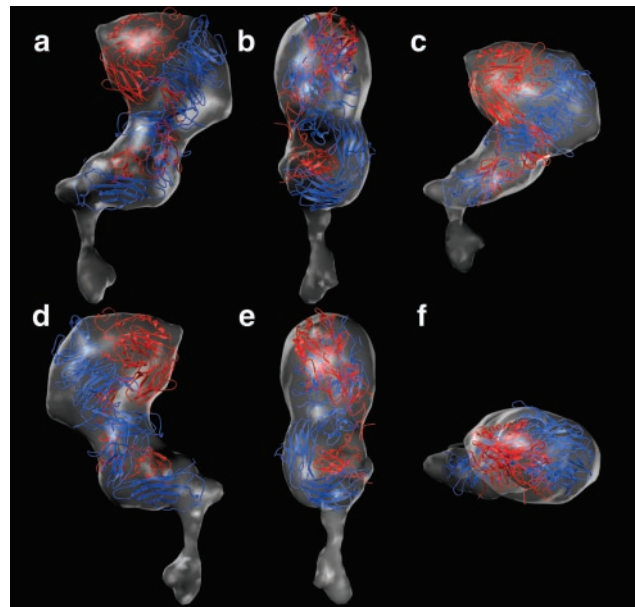


Fig. 4. Docking of the x-ray structure of the $\alpha_v\beta_3$ ectodomain into the map of $\alpha_{11b}\beta_3$ derived by electron cryomicroscopy and image analysis. (a) Same view as in Fig. 2. With a as a reference and viewed from above, b is rotated clockwise by 90°. (c) Same view as a except tilted 45° toward the viewer. (d) Same as a but rotated 180°. (e) Same as b but rotated 180°. (f) Same as a but rotated 90° toward the viewer. Note the excellent fit of the domains within the x-ray structure to the EM map. In b and e, there is additional density outside of the fitted x-ray model, which may be due to disordered polypeptide not seen in the x-ray map. Because the α_{11b} and β_3 each have six carbohydrate-binding sites (33), we presume that part of this density may also be due to bound carbohydrate that is not included in the x-ray structure. On the basis of a comparison of the migration of the protein on SDS gels (Fig. 1a) with the molecular mass calculated from the sequence, we estimate 20% glycosylation.

tative transmembrane domains and an extracellular Ig-like domain (30). Although direct association has not been demonstrated, the stalk region could easily accommodate interactions with both an Ig-like domain and the large extracellular loop of TM4SF.

In the Low-Affinity State, the Cytoplasmic Domains of α_{11b} and β_3 Are Associated. At the end opposite the head domain is a bilobed, inverted heart-shaped density that accounts for ≈ 7 kDa. Because this mass is close to the combined cytoplasmic domains of α_{11b} and β_3 , we interpret this density as the associated C-tail domains of the α_{11b} and β_3 subunits. We presume that the larger lobe of density corresponds to β_3 , because its cytoplasmic domain is about twice the size of the α_{11b} cytoplasmic domain. If so, the cytoplasmic domain of the β_3 subunit is roughly colinear with the transmembrane rod of density (Fig. 2). A recent NMR study of recombinant cytoplasmic domains of α_{11b} and β_3 (35) suggested a tendency for residues 724–735 in the β_3 tail to form an α -helix, which might be an extension of the transmembrane α -helix.

The Transmembrane Domains Associate as an α -Helical Coiled-Coil. The cylindrical transmembrane density that connects the small cytoplasmic domains with the large ectodomain is sufficiently long (≈ 30 Å) to span the hydrophobic barrier of the membrane (Fig. 2). Earlier images of dried and platinum shadowed samples (11) showed two threads of density thought to correspond to the stalks of α_{11b} and β_3 that connect to the transmembrane domains. Our map, derived from frozen-hydrated particles, suggests that the transmembrane domains are associated, which would thereby juxtapose the immediately adjacent cytoplasmic domains. This interpretation agrees with recent mutational data (36). At 20-Å resolution, the shape of the rod corresponds to that expected for a

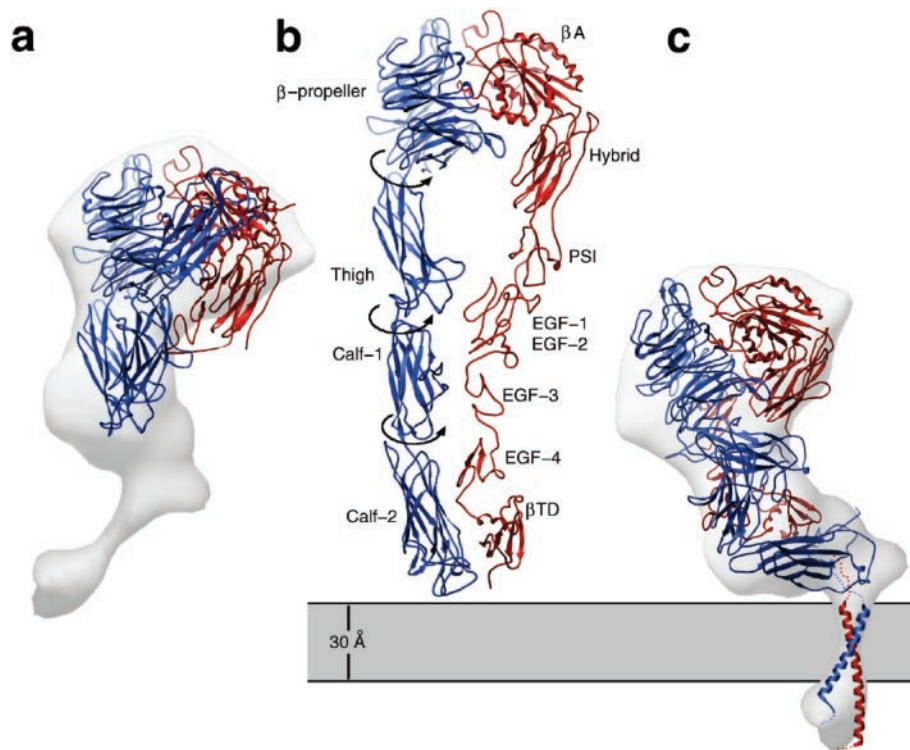


Fig. 5. Ribbon models depicting (a) the x-ray crystal structure of the $\alpha_v\beta_3$ ectodomain, (b) an extended model of the putative high-affinity state (21), and (c) the model for $\alpha_{IIB}\beta_3$ in the low-affinity state based on Fig. 4. The α and β polypeptide chains are colored blue and red, respectively. The 12 domains in the extracellular portion of $\alpha_v\beta_3$ are labeled in b according to Xiong *et al.* (21). Superposition of the map derived by electron cryomicroscopy shows a much better fit to the ribbon model shown in c versus the x-ray structure (a). The low-affinity state (c) can be generated from the putative high-affinity state (b) by rearrangements between Ig-like domains that would be analogous to bending at elbow angles in Fab molecules. This hinging at three pivot points would shorten the structure by ≈ 80 Å and would move the head into proximity with the membrane surface. The map of $\alpha_{IIB}\beta_3$ (Fig. 2) shows that the transmembrane domains are associated as a single rod of density, which have been modeled as a right-handed, parallel, α -helical coiled-coil (c). We interpret the larger lobe of the cytoplasmic domain in Fig. 2 as the β_3 cytoplasmic tail, which is about twice the size of the α subunit cytoplasmic tail. On the basis of NMR spectroscopy (39), the first 11 residues in the β_3 cytoplasmic tail adopt an α -helical conformation, and if they are a continuation of the transmembrane helix as depicted in c, then this region of β_3 may function as a lever arm to elicit cytoplasmic conformational changes.

parallel, α -helical coiled-coil; however, the hand of the coiled-coil is uncertain (data not shown).

Several membrane proteins fold with transmembrane α -helical coiled-coils that have well packed interfaces sensitive to mutations (37). For the integrin superfamily, β_3 will pair with α_{IIB} or α_V , whereas α_V will dimerize with β_1 , β_3 , β_5 , β_6 , and β_8 (6). Homology within the α and β subunits suggests that the tertiary folding of the two polypeptides will be conserved for different isoforms. If so, we reasoned that the dimer interface should be conserved between all of the permitted $\alpha\beta$ pairs in this series. To explore this idea, we modeled the α and β transmembrane domains as a canonical left-handed leucine zipper motif (Fig. 3b) and as a right-handed coiled-coil (Fig. 3c). Mutational analysis suggests that R995 in α_{IIB} and D723 in β_3 form a salt bridge (36). Therefore, we used these residues to rotationally align the transmembrane α -helices. Modeling the α -helices as a canonical left-handed coiled-coil (Fig. 3d) places some of the conserved residues at the protein-protein interface. However, for the right-handed coiled-coil, many more of the absolutely conserved residues are at the interface (Fig. 3e).

Comparison Between the Ectodomains of $\alpha_{IIB}\beta_3$ in the Low-Affinity State and the Crystal Structure of $\alpha_V\beta_3$. Because the β_3 polypeptides are identical and the α_V and α_{IIB} polypeptides exhibit 36% identity and 50% homology, we felt justified in using the x-ray structure of $\alpha_V\beta_3$ to derive a hypothetical model for the ectodomain of $\alpha_{IIB}\beta_3$. In the x-ray structure, there is a severe $\approx 130^\circ$ bend between the head and the stalk. This “jack-knifed” conformation of the extended tails of $\alpha_V\beta_3$ did not fit the “neck” and “body” of our 3D

electron cryomicroscopy map (Fig. 5a). Consequently, the domains within the $\alpha_V\beta_3$ structure were visually fitted into the molecular envelope of the EM map of $\alpha_{IIB}\beta_3$ (Fig. 4) by a series of rigid body movements by using the programs O (29) and AVS (24). The modeling was constrained by the need to place (i) the RGD-binding site [between the β propeller domain and the βA domain (38)] in the head region, (ii) the C termini of both the α and β chains adjacent to the putative transmembrane rod, and (iii) the Ig-like calf I domain close enough to the membrane to allow potential interactions with tetraspanins (32). No intradomain changes were made, and the fitting avoided steric clashes between elements of secondary structure. However, the movements obviously required adjustments of connecting loops. The improvement in visual fit was supported by the computed *R* factors (0.48 and 0.32, comparing Fig. 5 a and c to the EM map, respectively).

Within the α subunit, a pivot at residues 438–439 between the β propeller and the Ig-like thigh domain (residues 439–592) rotated the thigh into the neck region of the EM map. This shift had the effect of moving the Ig-like calf-I domain (residues 602–738) into the neck, which was positioned vertically with respect to the membrane (as depicted in Figs. 2 and 5). A bend at residue 737 was required to position the Ig-like calf-II domain (residues 739–956) flush with the bottom of the body with its C terminus adjacent to the transmembrane rod.

The head of the EM map contained sufficient volume to accommodate the N-terminal region of the β subunit (residues 1–54, not seen in the crystal structure and not modeled here) as well as epidermal growth factor (EGF)-1 and -2. These domains (residues

453–529) were not well defined in the crystal structure. Consequently, they were modeled as a rigid body based on the structure of the EGF-3 and -4 domains. The EGF-3 and -4 domains (residues 532–605) were positioned across the neck and body, and the β tail domain (residues 606–690) was positioned in proximity to the membrane.

Implications for Integrin Activation. Despite impressive advances in the high-resolution structural characterization of integrin domains (21, 38–40), there continues to be controversy about the tertiary and quaternary changes associated with activation [reviewed by R. C. Liddington (41)]. The “jack-knifed” conformation of the $\alpha_v\beta_3$ ectodomain (Fig. 5a) is thought to result from a crystal packing artifact (21) because the membrane proximal “stalks” are folded back against the ligand-binding “head” domain. Nevertheless, a recent x-ray structure reveals that in this conformation, the head is still capable of binding a cyclic peptide with the RGD motif (38). On the basis of previous EM studies (19), it was suggested that in the high-affinity conformation, the tails of the two chains are rotated away from the putative ligand-binding site so that the entire structure would extend well above the membrane surface (Fig. 5b). Such a model is consistent with gel-filtration chromatography of detergent-solubilized $\alpha_{IIb}\beta_3$, in which a large increase in hydrodynamic radius occurs on ligand binding (11), and with fluorescence energy transfer measurements that indicate large domain movements on activation of $\alpha_{IIb}\beta_3$ (42).

Mutational analysis and antibody-binding studies have suggested that EGF-4 within the β_3 subunit mediates signal transduction (43). In addition, intrinsic thiol isomerase activity in the cysteine-rich repeats suggests that disulfide exchange may play an important role in signal transmission (44). How might the α chain participate in integrin activation? The proposed bending between the Ig-like domains to convert the extended conformation in Fig. 5b to the folded compact form in Fig. 5c would be analogous to bending at elbow connections in Fab molecules, which can range from ≈ 125 to $\approx 230^\circ$ (45, 46). The fairly low contact surface areas between the β propeller and the thigh ($\approx 700 \text{ \AA}^2$), the thigh and calf-1 (200 \AA^2), and calf-1 and calf-2 (500 \AA^2) (Xiong *et al.*, ref. 21), would suggest that rotations would be possible. Therefore, we propose that small tertiary rearrangements in the ligand-binding site are transmitted to the transmembrane domains by elbow angle-like bending between the Ig-like domains.

A possible sequence of rearrangements that would convert the extended form (Fig. 5b) to the compact form of the low-affinity

state (Fig. 5c) would involve (i) ligand binding in the vicinity of the β propeller and βA domains (Xiong *et al.*, ref. 38); (ii) changes in divalent cation coordination in the metal-ion-dependent adhesion site (MIDAS) (38, 40); (iii) associated small structural changes between the β propeller and βA domains, as has been observed with the I domain both bound to a collagen fragment and in the unliganded state (40); (iv) structural shifts between the β propeller and thigh domains; (v) amplification of the conformational changes by “elbow-angle” bending between the thigh, calf-1, and calf-2 domains; and (vi) propagation of these changes to the transmembrane coiled-coil. The changes in the angular relationships between the Ig-like domains would shorten the structure by $\approx 80 \text{ \AA}$ and would move the head into proximity with the membrane surface.

It is unclear how the large domain shifts within the stalks of the α and β subunits would be translated into movements of the transmembrane α -helices that culminate in conformational changes in the cytoplasmic domains. Nevertheless, the α -helical packing for the α and β transmembrane domains provides constraints for transmembrane signaling. A coiled-coil arrangement would be compatible with mechanisms that involve helix-coil transitions, helical rotation or scissoring, or helix dissociation with or without reassociation (16). However, a piston model in which the α -helices slide vertically against each other and break hydrogen bonds would be energetically unfavorable. A rotation or scissoring model is appealing because the α -helical extension of the β_3 tail could then serve as a lever arm to elicit cytoplasmic conformational changes.

Our study by electron cryomicroscopy, image analysis, and molecular modeling provides a new stanza in the orchestration of integrin signaling. Additional high-resolution structures and a map of the full length integrin in the presence of bound ligand are required to test the hypotheses that have been proposed by others as well as ourselves for the tertiary and quaternary rearrangements that accompany integrin signaling.

We thank Michael E. Pique for assistance in figure preparation and our colleagues at The Scripps Research Institute for comments on the manuscript. We gratefully acknowledge M. Amin Arnaut for helpful discussions and for providing the x-ray coordinates of $\alpha_v\beta_3$. This work was supported by the National Institutes of Health, National Heart, Lung, and Blood Institute (to M.Y.) and a postdoctoral fellowship from the California affiliate of the American Heart Association (to B.D.A.). During the course of this work, M.Y. was an Established Investigator of the American Heart Association and is now the recipient of a Clinical Scientist Award in Translational Research from the Burroughs Wellcome Fund.

- Humphries, M. J. (2000) *Biochem. Soc. Trans.* **28**, 311–339.
- Howe, A., Aplin, A. E., Alahari, S. K., & Juliano, R. L. (1998) *Curr. Opin. Cell Biol.* **10**, 220–231.
- Brooks, P. C., Clark, R. A. F., & Cheresh, D. A. (1994) *Science* **264**, 569–571.
- DeSimone, D. W. (1994) *Curr. Opin. Cell Biol.* **6**, 747–751.
- Price, D. T., & Loscalzo, J. (1999) *Am. J. Med.* **107**, 85–97.
- Hynes, R. O. (1992) *Cell* **69**, 11–25.
- Haas, T. A., & Plow, E. F. (1994) *Curr. Opin. Cell Biol.* **6**, 656–662.
- Du, X., & Ginsberg, M. H. (1997) *Thromb. Haemostasis* **78**, 96–100.
- Faull, R. J., Du, X., & Ginsberg, M. H. (1994) *Methods Enzymol.* **245**, 183–194.
- Vorhheimer, D. A., Badimon, J. J., & Fuster, V. (1999) *J. Am. Med. Assoc.* **281**, 1407–1414.
- Carrell, N. A., Fitzgerald, L. A., Steiner, B., Erickson, H. P., & Phillips, D. R. (1985) *J. Biol. Chem.* **260**, 1743–1749.
- Weisel, J. W., Nagaswami, C., Vilaire, G., & Bennett, J. S. (1992) *J. Biol. Chem.* **267**, 16637–16643.
- Wippler, J., Koums, W. C., Schlaeger, E. J., Kuhn, H., Hadvary, P., & Steiner, B. (1994) *J. Biol. Chem.* **269**, 8754–8761.
- Parise, L. V., & Phillips, D. R. (1985) *J. Biol. Chem.* **260**, 1750–1756.
- Chiu, C. Y., Mathias, P., Nemerow, G. R., & Weisel, J. W. (1999) *J. Virol.* **73**, 6759–6768.
- Plow, E. F., Haas, T. A., Zhang, L., Loftus, J., & Smith, J. W. (2000) *J. Biol. Chem.* **275**, 21785–21788.
- Giancotti, F. G., & Ruoslahti, E. (1999) *Science* **285**, 1028–1032.
- Schwartz, M. A., Schaller, M. D., & Ginsberg, M. H. (1995) *Annu. Rev. Cell Dev. Biol.* **11**, 549–599.
- Hantgan, R. R., Paumi, C., Rocco, M., & Weisel, J. W. (1999) *Biochemistry* **38**, 14461–14474.
- Takagi, J., Erickson, H. P., & Springer, T. A. (2001) *Nat. Struct. Biol.* **8**, 412–416.
- Xiong, J.-P., Stehle, T., Diefenbach, B., Zhang, R., Dunker, R., Scott, D. L., Joachimiak, A., Goodman, S. L., & Arnaut, M. A. (2001) *Science* **294**, 339–345.
- Yeager, M., Berriman, J. A., Baker, T. S., & Bellamy, A. R. (1994) *EMBO J.* **13**, 1011–1018.
- Zudger, S. J., Baldwin, P. R., & Chiu, W. (1999) *J. Struct. Biol.* **128**, 82–97.
- Upson, C., Faulhaber, T., Jr., Kamins, D., Laidlaw, D., Schlegel, D., Vroom, J., Gurwitz, R., & van Dam, A. (1989) *IEEE Comput. Graph. Appl.* **9**, 30–42.
- Dennis, M. S., Henzel, W. J., Pitti, R. M., Lipari, M. T., Napier, M. A., Deisher, T. A., Bunting, S., & Lazarus, R. A. (1989) *Proc. Natl. Acad. Sci. USA* **87**, 2471–2475.
- Du, X., Plow, E. F., Frelinger, A. L., III, O’Toole, T. E., Loftus, J. C., & Ginsberg, M. H. (1991) *Cell* **65**, 409–416.
- Marcinkiewicz, C., Vijay-Kumar, S., McLane, M. A., & Niewiarowski, S. (1997) *Blood* **90**, 1565–1575.
- Koums, W. C., Hadvary, P., Haering, P., & Steiner, B. (1992) *J. Biol. Chem.* **267**, 18844–18851.
- Jones, T. A., Zou, J.-Y., Cowan, S. W., & Kjeldgaard, M. (1991) *Acta Crystallogr. A* **47**, 110–119.
- Hemler, M. E. (1998) *Curr. Opin. Cell Biol.* **10**, 578–585.
- Kitadokoro, K., Bordo, D., Galli, G., Petracca, R., Falugi, F., Abrignani, S., Grandi, G., & Bolognesi, M. (2001) *EMBO J.* **20**, 12–18.
- Yauch, R. L., Kazarov, A. R., Desai, B., Lee, R. T., & Hemler, M. E. (2000) *J. Biol. Chem.* **275**, 9230–9238.
- Calvete, J. J. (1994) *Thromb. Haemostasis* **72**, 1–15.
- Indig, F. E., Diaz-Gonzalez, F., & Ginsberg, M. H. (1997) *Biochem. J.* **327**, 291–298.
- Ulmer, T. S., Yaspan, B., Ginsberg, M. H., & Campbell, I. D. (2001) *Biochemistry* **40**, 7498–7508.
- Hughes, P. E., Diaz-Gonzalez, F., Leong, L., Wu, C., McDonald, J. A., Shattil, S. J., & Ginsberg, M. H. (1996) *J. Biol. Chem.* **271**, 6571–6574.
- Lemmon, M. A., & Engelman, D. M. (1994) *Q. Rev. Biophys.* **27**, 157–218.
- Xiong, J.-P., Stehle, T., Zhang, R., Joachimiak, A., Frech, M., Goodman, S. L., & Arnaut, M. A. (2002) *Science* **296**, 151–155.
- Beglova, N., Blacklow, S. C., Takagi, J., & Springer, T. A. (2002) *Nat. Struct. Biol.* **9**, 282–287.
- Emsley, J., Knight, C. G., Farnsdale, R. W., Barnes, M. J., & Liddington, R. C. (2000) *Cell* **101**, 47–56.
- Liddington, R. C. (2002) *Structure (Cambridge, U.K.)* **10**, 605–607.
- Sims, P. J., Ginsberg, M. H., Plow, E. F., & Shattil, S. J. (1991) *J. Biol. Chem.* **266**, 7345–7352.
- Chen, P., Melchior, C., Brons, N. H. C., Schlegel, N., Caen, J., & Kieffer, N. (2001) *J. Biol. Chem.* **276**, 38628–38635.
- O’Neill, S., Robinson, A., Deering, A., Ryan, M., Fitzgerald, D. J., & Moran, N. (2000) *J. Biol. Chem.* **275**, 36984–36990.
- Padlan, E. A. (1996) *Adv. Protein Chem.* **49**, 57–133.
- Wilson, I. A., & Stanfield, R. L. (1994) *Curr. Opin. Struct. Biol.* **4**, 857–867.
- MacKenzie, K. R., Prestegard, J. H., & Engelman, D. M. (1997) *Science* **276**, 131–133.